Design and analyses of printable strain hardening cementitious composites with optimized particle size distribution

van Overmeir, Anne Linde; Figueiredo, Stefan C.; Šavija, Branko; Bos, Freek P.; Schlangen, Erik

DOI
10.1016/j.conbuildmat.2022.126411

Publication date
2022

Document Version
Final published version

Published in
Construction and Building Materials

Citation (APA)
van Overmeir, A. L., Figueiredo, S. C., Šavija, B., Bos, F. P., & Schlangen, E. (2022). Design and analyses of printable strain hardening cementitious composites with optimized particle size distribution. *Construction and Building Materials*, *324*, Article 126411. https://doi.org/10.1016/j.conbuildmat.2022.126411

Construction and Building Materials 324 (2022) 126411

Contents lists available at ScienceDirect

Construction and Building Materials

journal homepage: www.elsevier.com/locate/conbuildmat

Design and analyses of printable strain hardening cementitious composites with optimized particle size distribution

Anne Linde van Overmeir [a,*], Stefan C. Figueiredo [b], Branko Šavija [a], Freek P. Bos [b], Erik Schlangen [a]

[a] Department of Materials, Mechanics, Management & Design (3MD), Delft University of Technology, Delft, Netherlands
[b] Department of the Built Environment, Eindhoven University of Technology, Eindhoven, Netherlands

ARTICLE INFO

Keywords:
3DP-SHCC
ECC
Buildability
Pumpability
Strain hardening
3d concrete printing

ABSTRACT

Since the advent of three-dimensional concrete printing (3DCP), several studies have shown the potential of strain hardening cementitious composites (SHCC) as a self-reinforcing printable mortar. However, only a few papers focus on achieving sufficient buildability when developing printable SHCC. This study investigates the role of the particle size distribution (PSD) in relation to the buildability properties of the mixture in the fresh state and strain hardening properties in the hardened state. To this end 6 mixtures were designed based on optimal particle packing with the application of the Modified Andreasen and Andersen Model. The two mix designs showed the highest displacement at maximum stress were selected for further development of their fresh state rheological properties. This was achieved by addition of a viscosity modifying agent (VMA) and a super plasticizer (SP) and through material analysis by means of ram extrusion tests. Further fresh material characterization on the final two 3DP-SHCC mix designs was attained by the deployment of uniaxial unconfined compression tests (UUCT), Vicat tests and Buildability tests. After successful printing of the two SHCC composites, the compressive strength, the 4-point bending strength and the uniaxial tensile strength and strain were determined at an age of 28 days. The research shows that optimization of the PSD in a 3DP-SHCC mix design results in an improvement of the buildability, but can introduce decreased pumpability and strain hardening capacity.

1. Introduction

Three-dimensional concrete printing (3DCP) is one of the most common techniques of the additive manufacturing (AM) for concrete, in which the cementitious material is extruded layer upon layer, by a digitally controlled robot. This new construction technique makes it possible to structurally optimize the architectural design, resulting in more slender structures and more efficient use of the material. Additionally the technique potentially has economic benefits as it makes the use of formwork superfluous. This can speed up the production process and reduces formwork costs. However, despite the benefits that this additive manufacturing technique offers, it is not yet widely applied in practice, due to the multiple technical challenges that still need to be overcome [1–3], one being the mechanical properties of plain concrete, which is brittle by nature and lacks sufficient tensile strength. In traditional concrete this lack of tensile strength is overcome by the implementation of steel bar reinforcement. This provides the concrete with the required ductile behaviour needed to comply with modern building regulations, as it ensures structural integrity and safety. For 3dcp however, the implementation of steel bar reinforcement is not evident. Multiple studies have been conducted on the reinforcement of full size printed concrete elements, differing from the application of an external reinforcement frame [4], to the use of post tensioning pre-stressed reinforcement [5,6].

SHCC, also known as Engineered Cementitious Composite (ECC), is a relatively new material that was invented in the early 1990s [7]. The material derives its name from its strain hardening behaviour in hardened state. In addition, SHCC is also characterized by its high tensile ductility. These properties are the result of the formation of multiple microcracks when the SHCC element is subjected to an increasing tensile stress, which is achieved by the incorporation of micro fibres (> 1,5 vol%) as self-reinforcement. The performance of these fibres, and their ability to bridge microcracks in the brittle cementitious matrix, strongly depends on micromechanics between the fibre and the matrix. The interaction between matrix, fibre and matrix/fibre interface is essential in order to obtain a cementitious composite with strain hardening behaviour [8].

* Corresponding author.
E-mail address: A.L.vanOvermeir-1@tudelft.nl (A.L. van Overmeir).

https://doi.org/10.1016/j.conbuildmat.2022.126411
Received 19 October 2021; Received in revised form 24 December 2021; Accepted 9 January 2022
Available online 7 February 2022

Considering its favourable structural properties, several research groups are exploring the possibilities to develop printable SHCC, and promising mechanical results have been achieved [9–12]. In a recent publication on 3DP-SHCC, Li et al. [13] provided a clear overview on all the research conducted and the remaining challenges that still need to be tackled. In this article the role of mortar design and its processing are characterized as essential. The potential application of SHCC within 3D concrete printing poses a new challenge. The design of a printable cementitious mortar/concrete comes with additional requirements on the fresh material and mechanical properties in order to be printable. This has best been described by Le [14] who states that for a material to be applicable for 3D concrete manufacturing it must meet the following four requirements: pumpability, extrudability, buildability and open time. **Pumpability** is the requirement that is involved with pumping the mixture through a hose towards the extrusion nozzle. This requires certain fresh material properties, such as a sufficiently low viscosity and limited aggregate size. Furthermore the mixture should be stable in order not to segregate under pumping pressure, which can lead to blockage of the hose and the formation of fibre balls [15,16]. In regard to **extrudability**, the mixture should be stable when the layer is extruded from the nozzle, with limited cross-sectional deformation and imperfections in terms of tearing. Then there is the requirement of **buildability**, which specifies that the layer should be able to resist its own weight as well as the weight of subsequently added layers. **Open time** is the period between the mixing of the mortar and the loss of printability. This loss of printability is related to the time dependent increase of the yield strength due to the formation of hydration products.

In continuation of this, Roussel [17] presented the rheological requirements for a printable concrete mix. The article provides a clear overview of rheological parameters, printing parameters and printing failure parameters that influence the printing process . The contradicting fresh mechanical properties that are required for pumpability and buildability is where the challenge lies for designing printable mortars.

To achieve the required rheological parameters like critical yield stress and plastic viscosity, use can be made of admixtures like superplasticisers, viscosity modifiers, retarders and accelerators. [18]. However, where tailoring of the concrete mix to fit the printability requirements is a good approach, for SHCC this brings new challenges. Optimization of the fresh properties with admixtures can jeopardize the requirements regarding the strain hardening behaviour. A good illustration hereof is the research conducted by Figueiredo et al. [10,19] on refining the rheological properties of a known SHCC mix design (M6), originally designed by Zhou et al. [20]. The result was a mix that satisfied the requirements of pumpability, extrudability and open time, but showed insufficient buildability for 3D printing applications. Furthermore, the strain hardening behaviour of the composite in hardened state had been compromised. Due to the tweaking of the rheological properties, by the addition of SP and VMA, the tensile strain at maximum stress decreased from 3.3% to 0.26% and the flexural deformation was reduced from 3.8 mm to 2.75 mm. The article suggested that the use of high amounts of viscosity modifying agents (VMA) to achieve sufficient yield stress and viscosity has led to high porosity. This high content of air voids had weakened the matrix and the matrix/fibre interface, which resulted in the limited strain hardening capacity.

In literature it is suggested that the solution to the contradicting printing requirements can to a certain extent be found in the structural build-up behaviour of the material and hence the material composition and the particle packing of the granular ingredients [21]. The current research focusses on the material design of 3DP-SHCC and aims to find a systematic approach to design a printable and strain hardening cementitious composite.

To this end 6 mixtures were designed based on optimal particle packing. These six mixtures were mechanically tested on flexural strength and deformation by use of a 4-point bending test. The two mix designs that showed the best performance were selected for further development of their fresh state rheological properties. This was done by the adding of VMA and (additional) SP and the rheological properties were quantified by means of a ram extruder. Further fresh material characterization of the final mixtures was achieved by the deployment of uniaxial unconfined compression tests (UUCT) and Vicat tests. Subsequently, both mixtures were subjected to a printing trial including a buildability test, to observe their performance on the printability requirements; pumpability, extrudability, buildability and open time. The beams resulting from these printing sessions have been subjected to mechanical tests at an age of 28 days, to assess their compressive strength, 4-point bending strength and uniaxial tensile strength and strain. The underlying hypothesis is that the PSD optimized mix designs yield good buildability properties and shows strain hardening behaviour under uniaxial tensile loading.

2. Theory

Fresh concrete can be characterized as a Bingham fluid, also known as a yield stress fluid, meaning that fresh concrete behaves as a solid when the applied stress is below a critical yield stress, and behaves like a liquid when a stress is applied above this critical value [22,23]. Additionally, the rheological properties of fresh concrete mixtures are dependent on its flow history. For fresh concrete, it can be stated that with increasing time in state of rest, the critical yield stress to initiate flow increases. This is due to the build-up of a stress-transferring structure between particles, a phenomenon that is called thixotropy.

It is suggested that [21] thixotropy is governed by two main mechanisms: re-flocculation and structuration. Re-flocculation is a physical process resulting from interparticle forces that grow structurally stable flocs and structuration is related to the formation of early hydration products of the cementitious particles. In relation to the phenomenon of re-flocculation, research has been conducted on the influence of particle size distribution (PSD). When the structurally stable flocs settle in an optimally packed particle microstructure, it will enhance the yield shear stress of the material which will result in better buildability for 3DCP [24]. Studies on the influence PSD by the use of small scale particles like nano-clay and silica fume show that the thixotropic behaviour increases when these particles are used [24–26]. Additionally, good particle size packing also enables the design of a stable mixture that will resist dynamic segregation during pumping [27].

Thus, for the development of a printable SHCC mix design that is sufficiently buildable, the optimization of the particle packing is an important objective. In order to achieve a sufficient particle packing the relative volumes of the ingredients must be determined accordingly, this can be achieved by the use of a particle packing model. In literature, two types of particle packing models can be defined namely, *discrete models* that take into account discrete size classes of two or more particles and *continuous models* that assume that all possible sizes are present in the particle distribution system [28]. In the context of concrete mix design the continuous models are preferred, as they can easily represent the continuous character of a mix design's particle size distribution. The modified Andreasen and Andersen (A&A) model, developed by Funk and Dinger, [29] is a continuous model that takes into account a minimum and a maximum particle size. This model has been widely applied to optimize the particle structure for different types of concrete, including, SCC [27,30], SH-UHPC, [31], UHPC [32], sustainable concrete [33] and printable mortars [34]. The modified A&A model is given in Eq. (1) and (2).

$$P_{tar}(D) = (D^q - D^q_{min})/(D^q_{max} - D^q_{min}) \quad (1)$$

$$P_{mix}(D) = \sum(v_i * PSD_i) \quad (2)$$

D = Particle size [μm]
D_{max} = Maximum particle size [μm]
D_{min} = Minimal particle size [μm]
q = Distribution modulus [–]
$P_{tar}(D)$ = Ideal volume fraction of particles smaller than D
$P_{mix}(D)$= Real volume fraction of particles smaller than D
v_i = Volume of mix ingredient i
PSD_i = Specific particle size distribution of mix ingredient i

In the modified A&A particle packing model the parameter q defines the curvature of the particle size distribution of the mix design. In general it can be stated that high values of q (0.4–0.6) result in less workable mixtures that contain limited fines and high fraction of aggregates.

Combining Eqs. (1) and (2) together with a least square analysis results into the most optimal composition of the mix, given the chosen distribution modulus.

3. Materials

For the development of a printable SHCC mix design that has sufficient buildability properties, the optimization of the particle packing was taken as the backbone of the research.

The methodology of mix design and selection is as follows:

1. Six trial mixtures are designed using the modified A&A particle packing model.
2. Based on mechanical properties retrieved from a 4-point bending test, two of the designed trial mixes will be selected for further development.
3. These two mix designs are developed further by adding of VMA and SP to improve the rheological properties.
4. The improved mix designs with the most optimal rheological solution are then selected and renamed as mix A and mix B.
5. Fresh rheological properties are determined by means of ram extrusion tests, unconfined uniaxial compression tests and Vicat tests.
6. Printing sessions will be conducted, covering buildability tests and printing of the beams from which samples are extracted.
7. Hardened mechanical and material properties of the printed material will be determined by means of compression tests, 4-point bending tests, uniaxial tensile tests and CT scans.

Binders used in this study are: CEM I 42.5 N, CEM I 52.5 R, Blast furnace slag (BFS) and Silica fume (SF). SF has been used to increase small particle fraction, therewith aiming to increase the thixotropic behaviour. CEM I 52.5 R has been added to the research to bridge the gap in particle size range between SF and BFS. Particle size distribution curves were either received from supplier or measured by means of laser diffraction spectroscopy with a DIPA-2000 particle analyzer.

Fillers consist of Limestone powder (LS), Sand 125–250 μm, Sand 250–500 μm and Sand 500–1000 μm. To safeguard the strain hardening capacity of the 3DP-SHCC, no fillers with a size of > 1000 μm were used in this research.

For the material research two groups of binders and three groups of fillers were defined (see Table 1). The commonly used the Polyvinyl Alcohol (PVA) fibre was added to achieve strain hardening capacity [8]. Specifications on the mechanical properties of the specific RECS15 fibre can be found in Table 2.

With the use of the Modified A&A Model [35] the optimal particle size composition of all six combinations between binder and filler groups was calculated. The study utilized a maximal particle size (D_{max}) for Mix A and Mix B of 250 μm and 500 μm, respectively and a D_{min} of 0.05 μm. For the distribution modulus q a value of 0.25 was chosen, based on the findings in research conducted by Ragalwar et al. [32,36] on the most optimal q-value for UHPC-SHCC.

Table 1
Binder and filler groups.

Binder groups	BCS:	BFS + CEM I 42.5 N + SF
	BCCS:	BFS + CEM I 42.5 N + SF + CEM I 52.5 R
Filler groups	250:	LS + Sand 125–250
	500:	LS + Sand 125–250 + Sand 250–500
	1000:	LS + Sand 125–250 + Sand 250–500 + Sand 500–1000

Table 2
RECS15 fibre specifications.

		PVA (RECS15)
Tensile strength	(MPa)	1600
Modulus of elasticity	(Gpa)	41
Ultimate strain	(%)	6
Length	(mm)	8
Diameter	(μm)	40
Aspect ratio	(L/D)	200

Figures on the particle size distribution of the raw materials and of the mix design BCCS1000 are presented in Figs. 1(a) and 1(b) respectively. The final composition of the six dry material designs; BCS250, BCS500, BCS1000, BCCS250, BCCS500 and BCCS1000 can be found in Table 3.

The mixing was done on a Hobart A200-N planetary mixer, at a constant low speed (60 rpm). The procedure was kept the same for all 6 mix designs and consisted of the following steps:

– 2 Minutes: Mixing all dry materials, including fibres and SP
– 1 Minute: Adding of water while mixing
– 3 Minute: Mixing of wet material

In a later stage of the material development the methyl hydroxyethyl cellulose based VMA, Tylose MHS 15002 P6 was incorporated in the mix design. For these mixes adjustments were done to the mixing procedure.

– 2 Minutes: Mixing all dry materials, including fibres, SP and $\frac{1}{3}$ of the VMA.
– 1 Minute: Adding of water while mixing
– 1 Minute: Mixing of wet material
– Add: $\frac{2}{3}$ of the VMA.
– 2 Minutes: Mixing of wet material

The mixing procedures described above differ from the mixing process of general SHCC, where the fibres are added in the slurry phase. 3DP-SHCC is a very dough-like mixture, compared to normal SHCC. Due to this high viscosity of the fresh slurry, it is very difficult to disperse the fibres sufficiently when added in dough-like phase. The mixing procedure was therefore adjusted accordingly.

The developed mix designs have been cast and tested on 7-day flexural strength by means of a 4-point bending test with the aim to assess their deflection capacity and their potential strain-hardening behaviour. The performed 4-point bending test was chosen as it gives, in comparison to the uniaxial tensile test, more quantifiable data on mixes that do not have strain hardening capacity. Therefore the test is able to distinguish between a wider range of mix designs, with more or less strain hardening capacity.

The method utilized for the 4-point bending test and information on the sample sizes and curing conditions can be found in Section 4.

The results of the preliminary research on the mix designs with optimized PSD can be found in Table 4. Of the mix designs that showed flexural hardening behaviour, Mix BCS250 and Mix BCS500 showed the highest deflection capacity. These two mix designs have therefore been selected for further development of rheological properties, followed by the characterization of their fresh and hardened properties. This was done by an elaborate experimental program, of which the methods are described in Section 4.

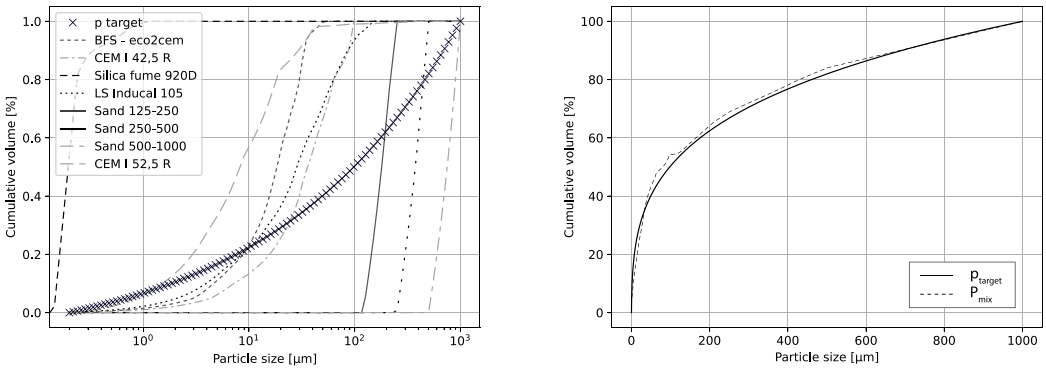

(a) PSD of raw materials (b) PSD of mix design BCCS1000

Fig. 1. PSD design with modified Andreasen and Andersen model.

Table 3
Mix composition.

		BCS			BCCS		
		250	500	1000	250	500	1000
Binder	Blast furnace slag	314	377	225	132	226	131
	CEM 1 42,5 N	483	458	500	478	502	522
	CEM 1 52,5 R	–	–	–	173	132	144
	Silica fume	70	51	40	60	41	39
Filler	Limestone powder	447	195	25	496	251	85
	Sand 125–250 µm	284	286	212	299	297	209
	Sand 250–500 µm	–	263	219	–	226	222
	Sand 500–1000 µm	–	–	231	–	–	235
Suppl.	Water	347	355	305	337	360	334
	Superplasticizer	1.73	1.77	1.53	1.69	1.8	1.67
	PVA (vol%)	2	2	2	2	2	2
Ratio	F/B	0.85	0.87	0.85	0.9	0.86	0.9
	w/b	0.4	0.4	0.4	0.4	0.4	0.4
	sp/b	0.2%	0.2%	0.2%	0.2%	0.2%	0.2%

4. Test methods

4.1. Overview experimental program

As described in Section 3 the selected mix designs BCS250 and BCS500 were developed further to tailor their rheological properties in respect to the printing requirements. This has been done by the employment of a ram extrusion test.

Afterwards the two mix designs, Mix A and Mix B, were subjected to a full printing session and an experimental program to assess their material and mechanical properties in fresh and hardened state. For the assessment of the fresh material and mechanical properties the mixtures were subjected to the following experiments: ram extrusion test, UUCT, open time test and buildability test.

The printed composites have been subjected to the following mechanical tests: Compressive test, 4-point bending test and uniaxial tensile test. Additionally, the 4-point bending test was conducted on cast samples to compare the mechanical performance of the cast versus the printed material.

Finally, a material assessment was done by the use of computed tomography (CT) to get insight into the internal micro-structure of a material, such as porosity over height and pore size.

4.2. Fresh properties: Ram extrusion tests

To achieve the rheological properties required for adequate pumpability and buildability, mix designs BCS250 and BCS500 were further developed with the incorporation of VMA and SP. To this end the ram extrusion test method was deployed according to the procedure of Figueiredo [10]. This ram extrusion method makes use of the non-linear Benbow–Bridgwater model for measurement data fitting and parameter determination as defined in Eq. (3) [37] .

$$P = P_1 + P_2 = 2\ln\left(\frac{D}{d}\right)(\sigma_0 + \alpha V^m) + \frac{4L}{d}(\tau_0 + \beta V^n) \quad (3)$$

P = Total pressure drop [kPa]
P_1 = Pressure drop in the die entry [kPa]
P_2 = Pressure drop in the die land [kPa]
σ_0 = Static yield stress [kPa]
α = Parameter characterizing speed in the die entry [kPa s/mm]
V = Extrusion speed in the die land [mm/s]
D = Barrel diameter [mm]
d = Die diameter [mm]
τ_0 = Shear yield stress [kPa]
β = Parameter characterizing speed in the die land [kPa s/mm]
L = Die length [mm]
m & n= non linear fitting coefficients

By varying VMA to binder ratio's and adapting the SP to binder ratio accordingly, the contribution of these additives to the rheological properties of the 3DP-SHCC has been assessed.

To determine the fresh mechanical properties *static yield stress* and *shear yield stress*, each mixture variant has been extruded through three different die lengths at 4 different speeds. Per die length a new batch of material was prepared to test the material at consistent age. Per die a minimum number of four ram extrusion tests were conducted, of which the average value was used for fitting of the Benbow–Bridgwater model. Results of these tests can be found in Section 5.1. Based on these results, the decision has been made to continue the research with two mixtures namely, mix BCS250 consisting of a VMA/binder ratio of 0.6% and a SP/binder ratio of 0.4%, and mix BCS500 consisting of a VMA/binder ratio of 0.4% and a SP/binder ratio of 0.3%. Throughout the rest of the paper these mixtures will be addressed as Mix A and Mix B, respectively. When including the new values for VMA and SP to the composition as given in Table 3 the final composition of the two 3DP-SHCC mix designs are as presented in Table 5.

4.3. Fresh properties: Uniaxial unconfined compression test

In this research a modified uniaxial unconfined compression test (UUCT) was used to determine the green compression strength of the printable mortar. The method has been developed by Wolfs et al. [38] and is based on the traditional UUCT standard for soil specimens, ASTM

Table 4
4-point bending test results, preliminary research.

	BCS250	BCS500	BCS1000	BCCS250	BCCS500	BCCS1000
Maximum flexural stress [MPa] (RSD)	10.77 (4.4%)	6.42 (12%)	5.76 (14%)	10.05 (10%)	9.08 (34%)	6.10 (22%)
Deflection at max. stress [mm] (RSD)	3.94 (18%)	3.22 (21%)	2.63 (20%)	1.66 (7%)	1.88 (82%)	1.47 (27%)

Table 5
Final composition Mix A and Mix B.

	BFS	CEM 42,5N	SF	LS	Sand 125–250	Sand 250–500	Water	PVA	SP	VMA
Mix A	314	483	70	447	284	–	347	26	3.47	5.20
Mix B	377	458	51	195	286	263	355	26	2.66	2.66

D2166 [39]. During the test the deformation of the sample is captured with an optical camera. With the use of National Instruments Vision Builder the optical data is post-processed and the load dependent cross sectional area is obtained. When the UUCT is performed at several time intervals after mixing, it can characterize the initial yield strength and its development over time. Meanwhile, also the initial apparent Young's modulus and its time development can be obtained from the acquired data.

The UUCT is performed on a cylindrical sample with a diameter of 70 mm and a height of 140 mm. The samples are made with the use of a steel mould that on the inside is covered with baking paper, to avoid the fresh material to stick. The sample was removed from the mould seconds prior to the testing of the sample. The sample is then placed in a Instron 5967 testing system, where a load cell with a 70 mm diameter loading plate is used to transfer the vertical compressive force onto the sample. The test was performed in displacement controlled mode, with a displacement rate of 0.5 mm/s. The test is carried out at $t = 5, 15, 30, 60$ and 90 min after mixing.

4.4. Fresh properties: Initial setting time

The open time of the mixtures is researched by means of a Vicat penetration test. From the cross relation of both test it was found that the initial setting time of mix A and mix B are equal to ± 3h30 and ± 4h30 respectively.

4.5. Fresh properties: Printing session and buildability test

4.5.1. Print facilities and settings

The printing facilities at the Delft University of Technology use a gantry system for creating the contour of the printed elements. The gantry system in Delft is illustrated in Fig. 2(a), and is able to print a volume of 1 * 0.6 * 0.35 m^3. The printing facilities are equipped with a PFT Swing M pump, which is connected to a 5 m hose provided with a down flow nozzle. The hose has a diameter of 25 mm, and the nozzle has a rectangular cross-section of 40 * 14 mm^2. A separate A200-N Hobart planetary mixer is used for preparing the 3DP-SHCC.

4.5.2. Printing session

A printing session has been conducted, composed of a buildability test and the printing of five beams of 800 mm length per 3DP-SHCC mixture. The beams consist of three 5-layer high beams and two 4-layer high beams and are printed in a back and forth printing routine as is presented in Fig. 2(b).

For the full printing session, 7 batches of 3.5 litres each were mixed as described in Section 3. As the material is prepared in multiple batches, the printing session could start after sufficient material was prepared. After preparation of each batch, the material was placed into the pump reservoir and covered with a plastic foil to prevent the mixture from dehydrating. After preparation of a sufficient amount the printing session started with a buildability test. For both mix A and B the buildability test started 40 min after the preparation of the first batch of material (see Table 6 and Table 7).

Table 6
Printing settings.

	Printing speed [mm/s]	Pumping speed [r.p.m.]
Mix A	20	72
Mix B	30	60

4.5.3. Buildability test

The buildability test is another method to characterize the fresh material properties of the 3DP-SHCC. This test differs from the other tests utilized for the determination of fresh mechanical properties, as it characterizes the material after completing the full printing procedure, instead of directly after mixing. In this study the buildability of the material was tested by printing a slender wall construction in subsequent layers of 800 mm length until it fails or maximum element height of the printer gantry is reached. Failure of the wall can occur either by plastic collapse or due to elastic buckling [40,41]. From the achieved layer height, the yield stress and apparent Young's modulus at time of collapse (from mixing) are calculated based on the theory provided by [42].

The apparent Young's modulus at time of failure $t = T$ can be calculated with:

$$l_{cr} = n_{layers} \cdot h_{layer} \cdot 10^{-3} \tag{4}$$

$$D_0 = \frac{l_{cr}^3 \cdot (\rho \cdot g \cdot b)}{(l_{cr}^*)^3} \tag{5}$$

$$E_{t=T} = \frac{12 \cdot D_0 \cdot (1 - \upsilon^2)}{h_{layer}^3} \tag{6}$$

The compressive yield stress at of failure $t = T$ can be calculated with:

$$l_p = n_{layers} \cdot h_{layer} \cdot 10^{-3} \tag{7}$$

$$\sigma_{c,t=T} = \frac{l_p \cdot \rho \cdot g}{l_p^*} \tag{8}$$

n_{layers} = Number of layers [–]
h_{layer} = Layer height [mm]
b = Width of layer [mm]
ρ = Density [kg/m^3]
g = Gravity [m/s^2]
l_{cr} = Critical buckling length [m]
l_{cr}^* = Dimensionless critical buckling length [–] = 1,99 for calculation E at time $t = T$ (not considering stiffness curing rate)
D_0 = Initial bending stiffness [Nm]
υ = Poisson's ratio [–]
$E_{t=T}$ = Young's Modulus at time of collapse $t = T$ [MPa]

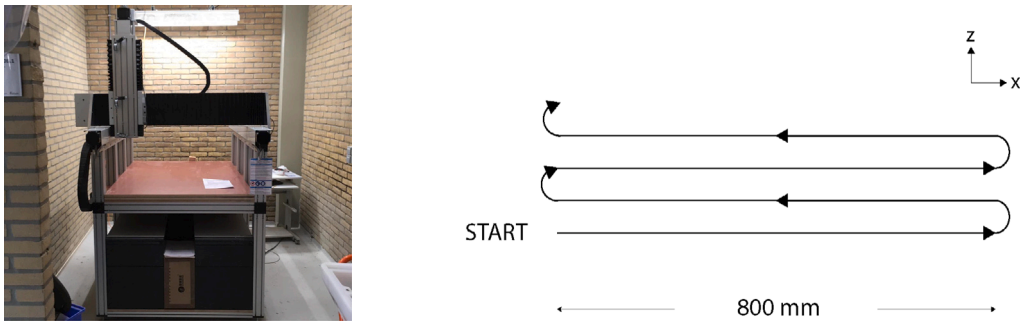

Fig. 2. (a) Printer facilities at TU Delft (b) Printing routing.

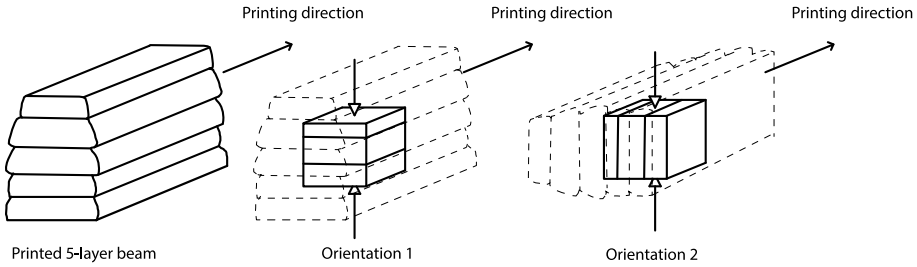

Fig. 3. Sample orientation of compressive test.

l_p = Plastic collapse length [m]
l_p^* = Dimensionless plastic collapse length [–] = 1 for calculation σ_c at time $t = T$ (not considering strength curing rate)
$\sigma_{c,t=T}$ = Compressive yield stress at time of collapse $t = T$ [kPa]

4.6. Hardened properties: 4-point bending test

The flexural strength was determined on cast and printed samples after 28 days. Both cast and printed test samples have a size of 30 mm (b) x 8 mm (h) x 150 mm (l). For the printed beams the height of 8 mm ensures the absence of an interlayer zone within the test sample. The samples have been cured at 20 °C with a relative humidity of 97% prior to testing.

All samples were tested in orientation 1 (load perpendicular to the printing plane), as Wolfs [38]. Tests were performed on an Instron 8872 servohydraulic testing system, in a displacement-controlled mode. The span of the test was 120 mm and the load was applied by two metal rods spaced 40 mm from each other. The deflection speed was set to 0.01 mm/s and two LVDTs measured the deflection in the middle of the span during testing.

4.7. Hardened properties: Compressive test

For the compressive test, cubes with an edge of 35 mm were sawn from the 5-layer high 3DP-SHCC beams. All test samples have been cured at 20 °C with a relative humidity of 97% prior to testing. To investigate the anisotropic behaviour of the printed SHCC, the compressive test was performed on orientation 1 (perpendicular to the layers) and orientation 2 (parallel to the layers), as can be seen in Fig. 3. Per orientation, a minimum of 5 test samples was tested on compressive strength at 7, 14 and 28 days after printing. The test was conducted in a servo hydraulic machine with a constant load rate of 2 KN/s in accordance with ASTM C-39 [43].

4.8. Hardened properties: Uniaxial tensile test

After seven days in the curing room, samples were sawn from printed SHCC beams using a wet stone saw with diamond powder coated blade. The samples had a rectangular shape with the following dimensions: 20 mm [w] × 40 mm [h] × 250 mm [l]. Fibre reinforced concrete, was cast on both outer ends to enlarge the cross-sectional area and therewith to ensure tensile failure to occur in the region with a smaller cross-section which was monitored during testing. An elaborate description on the sample preparation and test method can be found in authors previous work [44]. After 24 h the samples were demolded and placed back into the climate chamber to cure until testing.

The uniaxial tensile tests were carried out 28 days after printing in an Instron machine making use of the deformation-controlled mode. The displacement rate was set to 0.5 μm/s, resulting in a strain rate of 5 microstrain/s. Two LVDT sensors were utilized to measure the vertical displacement, the average value of the two sensors was used to control the vertical displacement of the tensile test. Full test set-up can be viewed in Fig. 4.

4.9. Material property: Porosity

To get insight in the air void content, the air void distribution and the presence of initial flaws in the printed strain hardening cementitious composites, two 20 mm diameter cores and two 40 mm diameter cores were extracted from the printed SHCC beams. The samples were subjected to X-ray CT scans with a Phoenix Nanotom X-ray. The 20 mm diameter samples were scanned with a resolution of 10 μm/pixel over a height of 20 mm. The scan was performed on the height of the second and the third layer. The acquired data was analysed for the determination of the air void content and distribution by the method that previously has been reported by van Overmeir and Figueiredo [19,44].

The 40 mm diameter cores were scanned with a resolution of 22.5 μm/pixel and the resulting images have been post processed with the use of VG studio software. The images were used to detect initial flaws, such as big entrapped air voids and the presence of fibre balls.

Table 7
Results ram extrusion tests.

	VMA/binder %	SP/binder %	σ_0, kPa	α –	m –	τ_0 kPa	β –	n –	
BCS250	0.30	0.40	1.14	4.07	0.60	0.15	0.10	0.45	
	0.45	0.40	3.54	16.40	0.33	1.06	1.00	0.56	
	0.60	**0.40**	**8.50**	**29.29**	**0.40**	**1.331**	**0.99**	**0.45**	**Mix A**
BCS500	**0.30**	**0.30**	**3.96**	**5.93**	**0.50**	**0.59**	**0.22**	**0.61**	**Mix B**
	0.45	0.30	6.77	10.23	0.41	0.52	0.53	0.50	
	0.60	0.30	7.99	30.95	0.34	2.01	0.171	0.69	

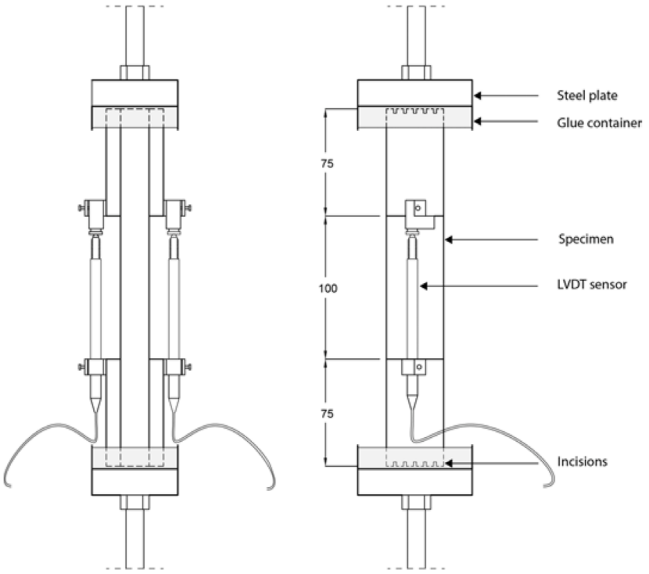

Fig. 4. Test set-up of tensile test.

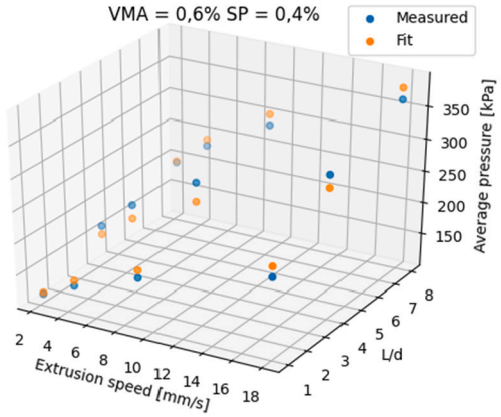

Fig. 5. Benbow–Bridgwater model fit on measured data for Mix A.

5. Results and analysis

5.1. Fresh properties

The ram extrusion test results that are presented in Section 5.1 show positive correlation between the static yield stress and the increase of the VMA to binder ratio. This trend is more pronounced for Mix A which contains more superplasticizer. The final design of Mix A and Mix B (shown in bold) have a static yield stress of 8.5 N/mm^2 and 4 N/mm^2, respectively.

To visualize the fit of the Benbow–Bridgwater model on the retrieved data, a 3D image plot of the average measured data and the model fit of Mix A is presented in Fig. 5.

The UUCT measures the compressive strength of the fresh composite at a given time. The average stress–strain curve from the three tested samples, are presented in Figs. 8(a) and 8(b) for Mix A and Mix B, respectively. Images of the test on mix A can be found in Figs. 6 and 7. The images and stress–strain curves display that the fresh printable SHCC samples have a different failure mechanism than printable mortars with no, or very small amounts, of fibres [38]. In this comparison two observations stand out, first one being the higher strain at maximum stress for the printable SHCC samples. Where the printable mixtures presented in [38] showed maximum stresses from ± 0.12% (at age of 5 min) to ± 0.2% strain (at age of 90 min), the 3DP-SHCC mixtures report maximum stresses from ± 0.2% (at age of 5 min) to ± 0.4% strain (at age of 90 min). The second observation that can be made is the difference in failure that occurs for the samples of 60 and 90 min. Where the low fibre content printable mortars display clear failure planes that correspond with failure planes of hydrated concrete under compressional force, the SHCC samples do not show these clear failure planes and the shape of failure is closer to those seen in the younger sample.

By performing the UUCT at multiple time intervals the development of the compressive strength over time has been obtained, these are presented in Figs. 9(a). By post-processing of the retrieved compressive stress values and their associated strain, the apparent Young's moduli could be determined. The results hereof are depicted in Fig. 9(b). Based on the results of the UUCT, the compressive strength and apparent Young's modulus for both material compositions a function can be defined for the first hours of the concrete after mixing. For Mix A this leads to Eqs. (9) and (10). In all equations the parameter t is set in minutes and σ and E are set in kPa.

$$\sigma_c(t) = 0.49 \cdot t + 8.04 \tag{9}$$

$$E(t) = 2.89 \cdot t + 66.26 \tag{10}$$

The Mix B the development of the compressive strength and apparent Young's modulus over time are represented in Eqs. (11) and (12).

$$\sigma_c(t) = 0.15 \cdot t + 0.55 \tag{11}$$

$$E(t) = 1.26 \cdot t \tag{12}$$

A striking result emerges from the trendline subjected to the average apparent Young's modulus values of Mix B, that predicts an initial Young's modulus of approximately zero for $t = 0$.

The compressive strength of Mix A at $t = 0$ was found to be 8.04 kPa, which is almost equivalent to the initial yield stress that resulted from the ram extrusion test, namely 8.5 kPa. This cannot be stated for Mix B, where the compressive strength at $t = 0$ of 0.55 kPa deviates strongly from the 3.96 kPa found in the ram extrusion analysis.

Both mixtures have been successfully printed on the printing facilities of Delft University of Technology. For Mix A the buildability test showed no failure at maximum height capacity of the printing gantry. The first 10 layers were printed with a consistent material flow and

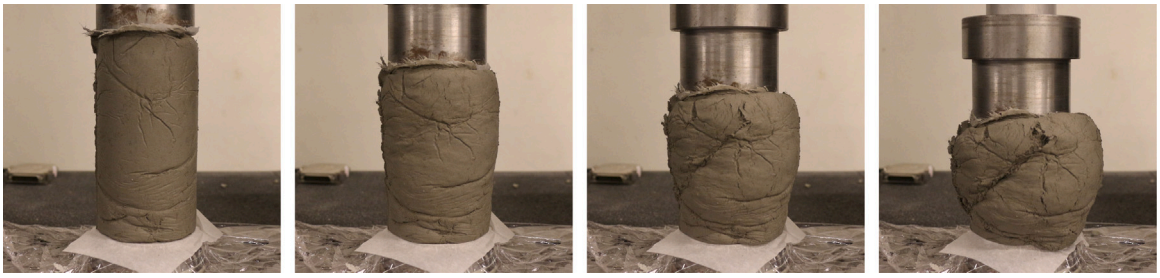

(a) 0% strain (b) 13.7% strain (c) 27.8% strain (d) 42.1% strain

Fig. 6. Images of UUCT for Mix A (60 min) with increasing vertical strain.

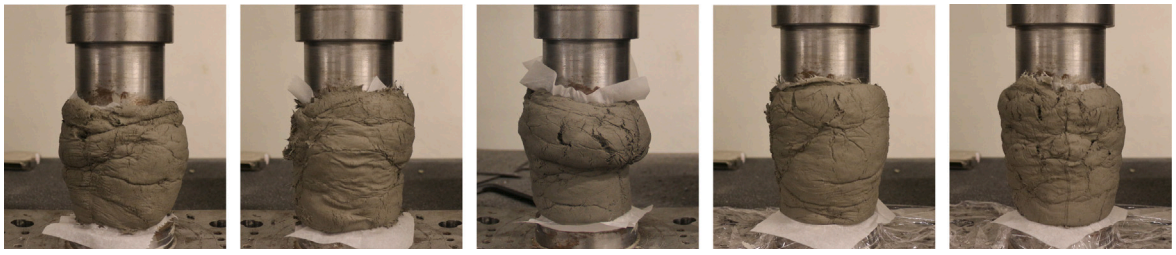

(a) 5 min (b) 15 min (c) 30 min (d) 60 min (e) 90 min

Fig. 7. Images of UUCT for Mix A of different ages with a constant vertical strain of 27.8%.

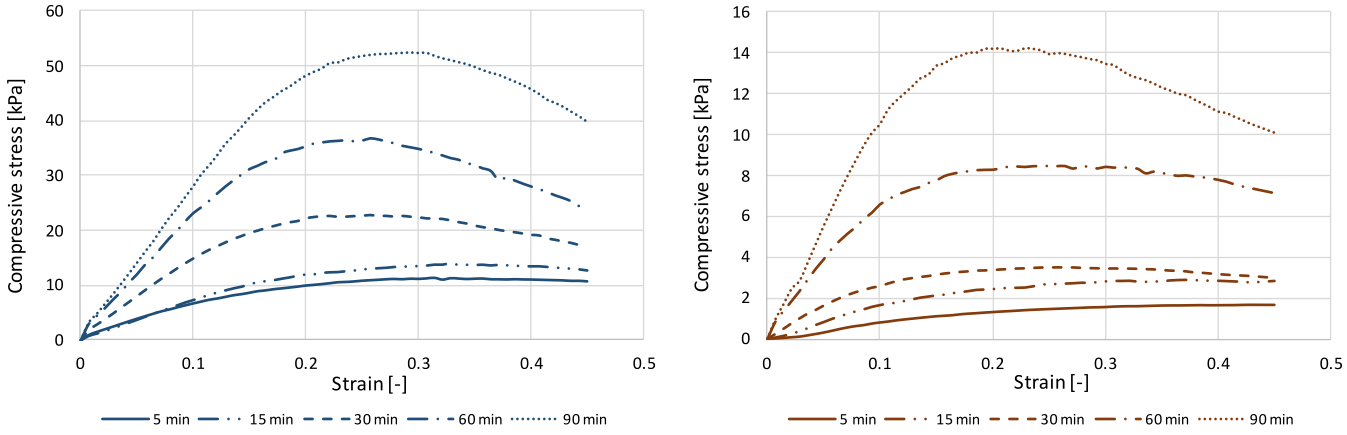

(a) Mix A (b) Mix B

Fig. 8. Average stress–strain curve of the uniaxial unconfined compression test. For clarity different Y-axis scales are for Mix A and Mix B.

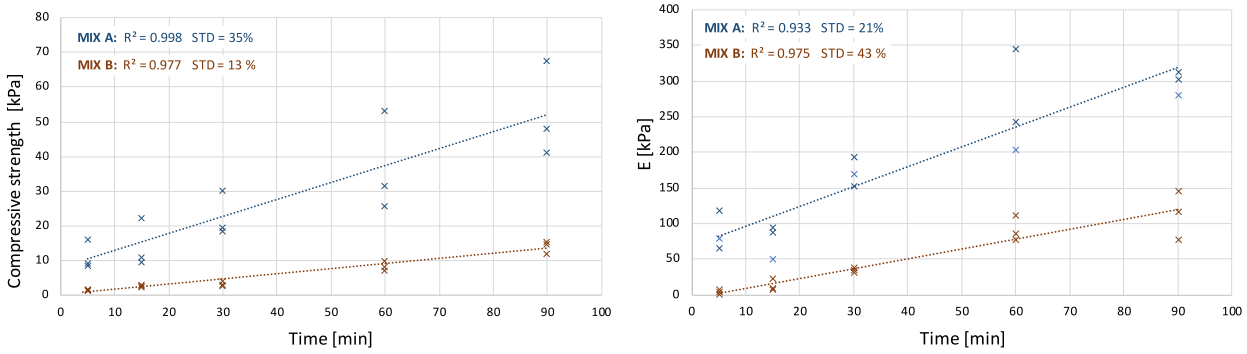

(a) Development of compressive strength over time (b) Development of Young's modulus over time

Fig. 9. Fresh mechanical property results from uniaxial unconfined compression test.

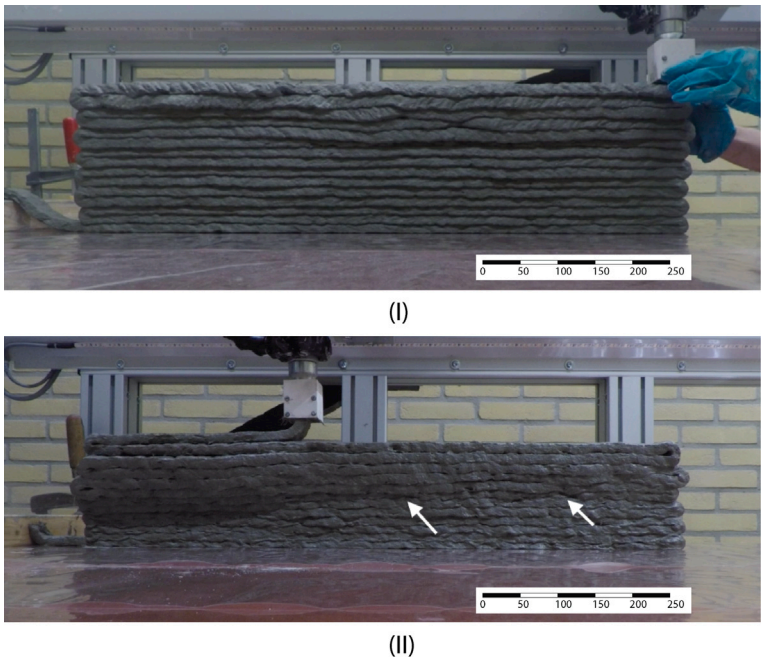

(a) Buildability test of Mix A (I) Mix B (II), scale in mm

(b) Top view Mix B, circles indicate air voids behind fibre balls

Fig. 10. Images of printing trial.

Table 8
Fresh properties from buildability test and UUCT.

		Buildability test		UUCT	
	Material age at time of failure T [min s]	$E_{t=T}$ [kPa]	$\sigma_{c,t=T}$ [kpa]	$E_{t=T}$ [kPa]	$\sigma_{c,t=T}$ [kpa]
Mix A	49.30	≥ 158.5	≥ 4.1	209.3	32.2
Mix B	43.20	103.0	≥ 3.6	54.6	6.8

stable layer shape, as can be observed in Fig. 10(a). The additional five layers (layers 10–15) show inconsistent and often excessive material flow, resulting in thicker layers consisting of wrinkles. This is most probably caused by the stiffening of the material in the pump reservoir. The maximum height of 210 mm was achieved in 9.5 min, which relates to a vertical wall growth velocity of 0.368 mm/s.

Mix B showed buckling failure at the beginning of the 13th layer after 6 min and 10 s, which yields to a wall growth velocity of 0.508 mm/s. All layers that were printed had a consistent material flow, nevertheless irregularities in layer shape can be observed in image II of Fig. 10(a). This was due to an unexpected observation, namely, the presence of fibre balls in the printed layers. These fibre balls are the result of segregation of the material during the pumping phase, as no segregation was observed after the mixing phase. Additionally, the printed layers showed lack of material directly extruded after the location of the fibre ball (in perspective of the moving nozzle). This is visible in the top view image of the printed elements in Fig. 10(b).

With the use of the Eqs. (4)–(8) and the time of failure (T) the minimal yield stress ($\sigma_{c,t=T}$) and elastic stiffness ($E_{t=T}$) at time of failure can be calculated. These values are presented in Table 8. The table also provides the corresponding yield stress ($\sigma_{c,t=T}$) and elastic stiffness ($E_{t=T}$) values at time of failure in accordance with the equations that were deducted from the strength development curves in Figs. 9(a) and 9(b).

Cross analysing the data of the UUCT with the calculated mechanical properties at time = T from the buildability test two things stand out. Firstly, the elastic stiffness of Mix B calculated from the buildability test is almost double the value that was found with the UUCT namely, 103.0 and 54.6 respectively. This offset is beyond the standard deviation that was found in the UUCT data. In effect, with the lower value for the Young's modulus determined with the UUCT, the buildability test would have resulted in buckling failure at the 11th layer. This contradicts the findings from the buildability test, where buckling failure occurred at a height of 13 layers. As the buildability test did not result in failure for Mix A, the buildability test only results in a minimum elastic stiffness of 158.5 kPa. This is in correspondence with the 209.3 kPa that was found for Mix A in the UUCT, which would have resulted in a maximum building height of 17 layers.

Secondly, the UUCT values for the compressive strength are significantly higher than needed for the achieved height. This has been visually confirmed, as no plastic deformation was observed at the lower layers during execution of the buildability test.

5.2. Hardened properties

All tested samples delivered flexural hardening in orientation 1 (load perpendicular to the printing bed), as shown in Fig. 11. From the supplied graphs it can be observed that the cast composites outperformed the printed composites in terms of flexural strength and the associated ductility. For the printed samples the flexural strength was reduced by 22.4% and 16.9% for Mix A and Mix B, respectively, in comparison with cast samples. The reduction in deflection capacity stands out even more, with a reduction of 63.1% and 42% (see Table 9).

The results from the compression test are presented in Fig. 12. From the 28 days test results it can be concluded that Mix B has a 10% higher compressive strength than Mix A. This result was expected as Mix B contains a higher amount of sand. Additionally, the orientation of the sample did not significantly influence the compressive strength. For the two tested orientations the differences are small and seem to fall within the error margin. However, when looking at the compressive

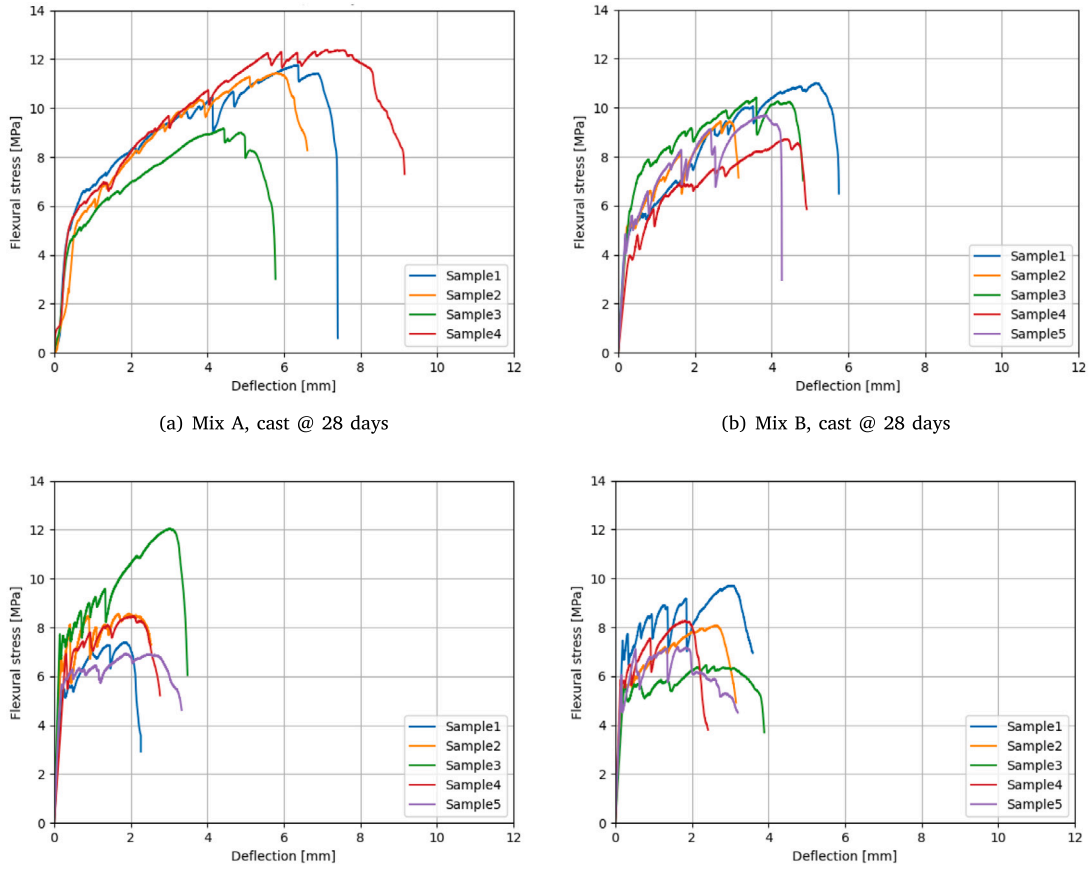

(a) Mix A, cast @ 28 days

(b) Mix B, cast @ 28 days

(c) Mix A, printed @ 28 days

(d) Mix B, printed @ 28 days

Fig. 11. 4-point bending: Flexural stress–deflection curves.

Table 9
4-point bending average values.

	MIX A			MIX B		
	Cast 28 days	Printed 28 days	Printed/ Cast	Cast 28 days	Printed	Printed/ Cast
Maximum flexural stress [MPa] (RSD)	11,18 (13%)	8,68 (23%)	−22.4%	9,56 (9%)	7,94 (15%)	−16.9%
Displacement at max. stress [mm] (RSD)	5,8 (19%)	2,14 (23%)	−63.1%	3,93 (24%)	2,28 (26%)	−42.0%

strength development over time, as shown in Figs. 12(a) and 12(b), it can be concluded that the compressive strength values of orientation 2 are systematically higher than orientation 1. This holds for both Mix A and Mix B.

In Fig. 13 the tensile stress–strain curve of the uniaxial tensile tests of both mixtures are plotted. What stands out from Fig. 13(a) is the high scatter in results from Mix A, where only two samples show strain hardening behaviour up to a strain of 1,5%. In test results of Mix B, presented in Fig. 13(b) illustrates that none of the samples show strain hardening. This was to be expected after the formation of the fibre balls during the printing procedure.

After sample failure, the fracture surfaces of the samples were inspected and it was found that a majority of those fracture surfaces contained big entrapped air voids. An image of one of these fracture surfaces and corresponding failure crack is presented in Fig. 14. These entrapped air voids were found, in various amounts, in all tested samples of Mix B and in the samples of Mix A, except for samples 2, 3 and 5. It is therefore plausible that these initial flaws are responsible for the lack of (Mix B) or variety in (Mix A) strain hardening response of the printed samples.

5.3. Material properties

Results of the air void content and distribution of the 20 mm diameter samples are shown in Figs. 15(a) and 15(c). In these figures the interlayer between the second and third layer is indicated with a black dashed line. From the porosity curves one main aspects stand out, being the high variation of the air void content over the sample height, for both mixtures, even though the average air content of composite A and composite B is similar, namely 5% and 6% respectively. For Mix A the air void content across the layer height varies between 3.5 and 9.8%. Mix B shows an even stronger variation, between 2.2 and 14.8%. In Figs. 15(b) and 15(d) the average pore diameter over height is presented for Mix A and Mix B, respectively. From these results no clear relation was found between the average pore diameter and the presence of the interlayer. Fig. 15(d) does present a higher average pore size in the centre of the analysed layers two and three. This, on first

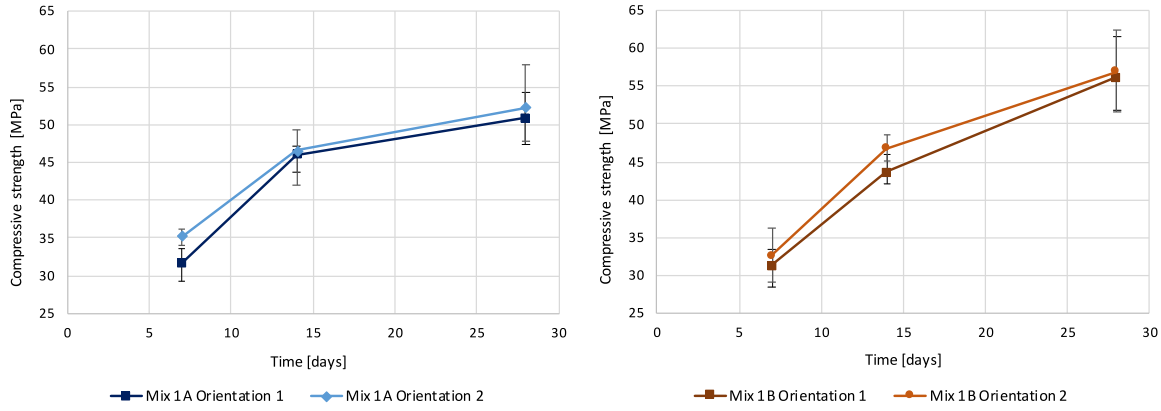

(a) Mix A (b) Mix B

Fig. 12. Compressive strength development over time.

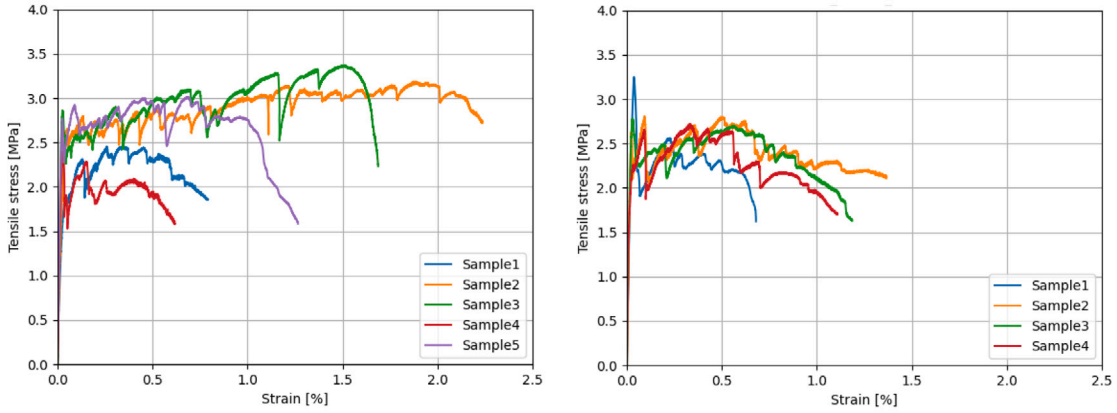

(a) Mix A (b) Mix B

Fig. 13. Stress–strain diagram uniaxial tensile tests.

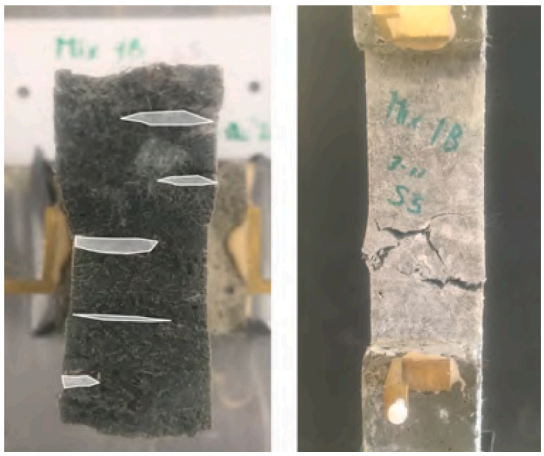

Fig. 14. Entrapped air voids visible on fracture surface of uniaxial tensile test sample 3, Mix B.

hand, does not correspond with the low air void content measured on that height. A possible explanation is that there is one big entrained air void and just a few smaller air voids, which leads to an increase of the average pore diameter, but does not necessarily result in higher overall porosity.

The presence of big entrapped air voids has also been confirmed by the images retrieved from the CT scan of the 40 mm diameter samples. A set of these images has been selected to illustrate these imperfections and can be found in Fig. 16. On the cross sectional images zones of poor homogeneity can be observed for Mix B. The areas as marked in Figs. 17(b) and 17(c) are of a lighter grey, indicating a denser material. Furthermore, they possess very thin and narrow air voids and are often surrounded with big entrapped air voids. When we take into consideration the observed fibre balls during the printing session of Mix B and the air voids that subsequently followed these fibre balls in the printed filament, as was shown in Fig. 10(b), it is likely to assume that these fibre balls are present in the composite. Furthermore, it can be stated that this segregation during printing has led to significant imperfections that resulted in an inhomogeneous and non strain hardening material.

6. Discussion

The partial objective of the conducted research was to achieve a printable mixture that met all four requirements for printability, namely, **Pumpability**, **Extrudability**, **Buildability** and **Open time**, by optimizing the PSD.

Overall it can be stated that Mix A performed well in regards to extrudability, buildability and open time, but underperformed in terms of pumpability, due to stiffening of the material in the pump reservoir. The same observation can be made for Mix B, only here the pumpability was poor due to material segregation. This segregation

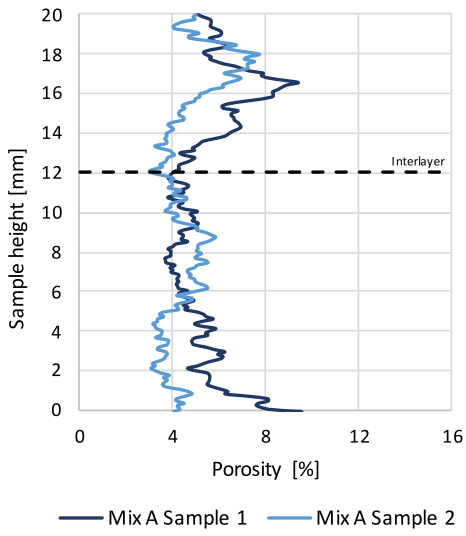

(a) Porosity over height, Mix A

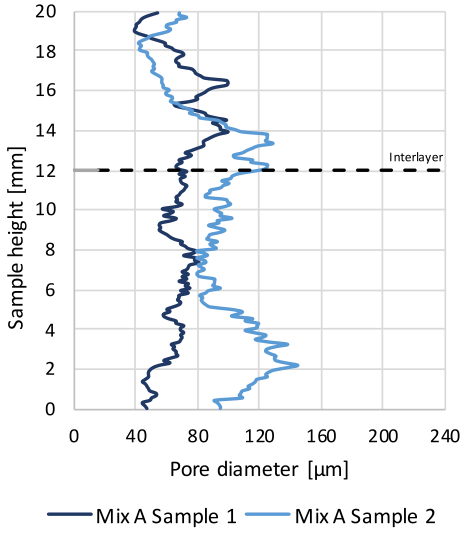

(b) Average pore size over height, Mix A

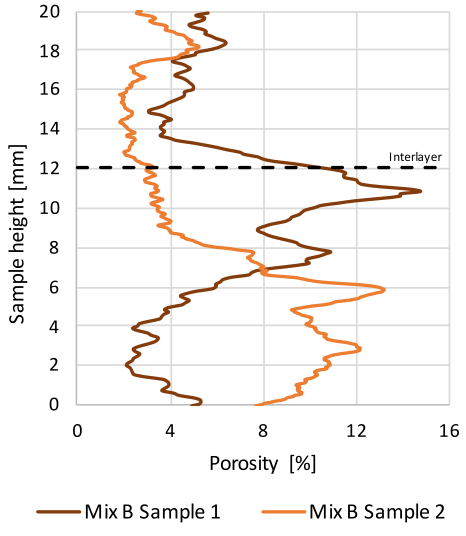

(c) Porosity over height, Mix B

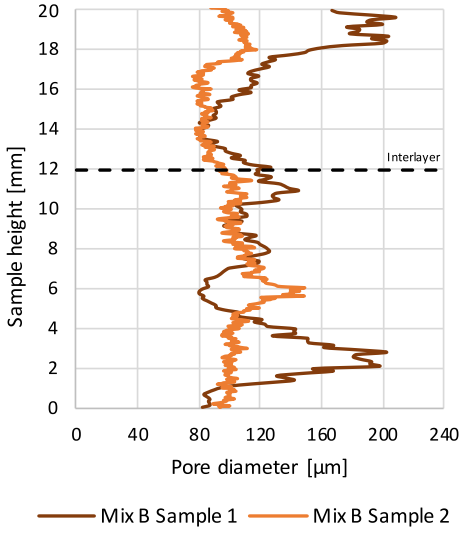

(d) Average pore size over height, Mix B

Fig. 15. Air void analysis.

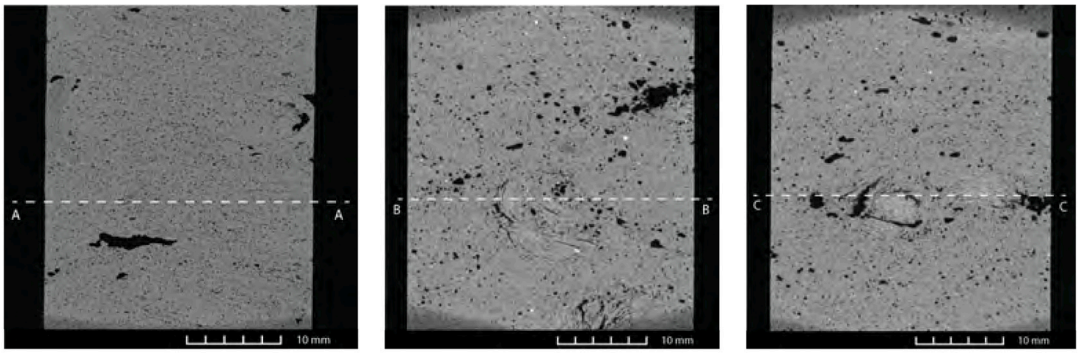

(a) Mix A, sample 1 (b) Mix B, sample 1 (c) Mix B, sample 2

Fig. 16. CT scan images.

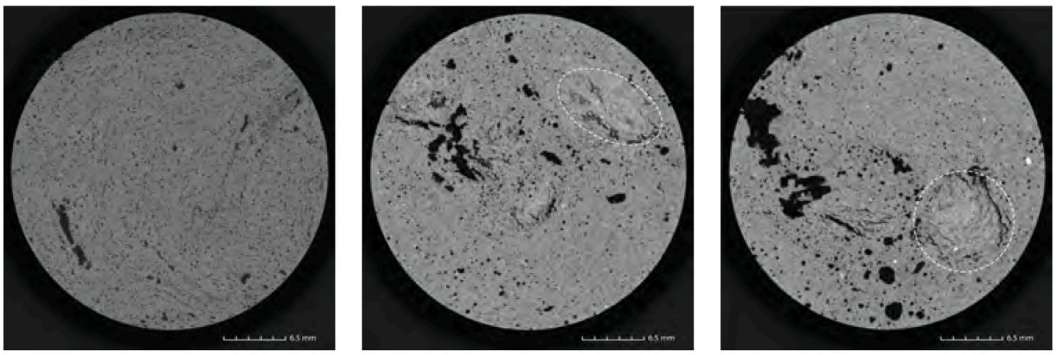

(a) Cross section A-A, Mix A (b) Cross section B-B, Mix B, circle indicates a fibre ball (c) Cross section C-C, Mix B, circle indicates a fibre ball

Fig. 17. Cross sectional images.

(a) Delft pump (b) Rotor/stator (c) Transport screw

Fig. 18. Pump configuration.

was an unexpected outcome of the printing trial, especially because a smooth and stable fresh 3DP-SHCC was achieved after mixing. The segregation resulted in the formation of fibre balls that led to inconsistent material flow and contributed to the weak strain hardening behaviour in hardened state. There are two possible causes for this segregation. On the one hand, it is possible that the segregation is caused by the high pressure cavity pump, where the geometry of the transport screw (in the material reservoir) and that of the rotor/stator in the pump may lead to formation of fibre balls. The pump configuration used in this research is presented in Fig. 18. On the other hand, the challenge may lie in the material design, since Mix A remained much more stable during the pumping process than Mix B. To the best of author's knowledge no literature on the topic of 3DP-SHCC has discussed segregation during pumping process. Therewith it should be noted that the use of a high pressure cavity pump for the application of 3DP-SHCC is not yet widely investigated.

Another interesting observation was the presence of air voids within the extruded layer. These big air voids were not observed during the printing trial, but were revealed after analysing the fracture planes of the tensile test samples.

This phenomenon was also observed by Figueiredo et al. [45], after conducting a printing trial on another type of 3DP-SHCC with the PFT Swing M pump. The hypothesis of Figueiredo et al. that states that the design of the transport screw causes these air voids to be entrained into the material, is in line with the findings of this research. Therewith, it should be emphasized that the pump geometry is of great importance when 3PD-SHCC is used for printing applications.

The segregation and entrapment of air voids are the two main reasons for the lack of (consistent) strain hardening results of Mix A and Mix B. For Mix A, the samples with no or limited amount of entrapped air voids were able to achieve strain hardening behaviour under tensile loading. Mix B, that besides the entrapped air voids, also contained fibre balls due to segregation, showed no strain hardening behaviour under tensile loading.

Relating the strain hardening performance under tensile loading to other research conducted on the development of SHCC for 3D printing as drawn up by Li et al. [13], we see that Mix A and Mix B underperform. However, it should be noted that the results presented by Li, are mostly based on samples printed with the use of caulk guns or Archimedes screw pumps. Comparing Mix A with the two other PVA reinforced composites that have been printed with the use of a high pressure cavity pump [10,19], the strain capacity under tensile loading has improved. Where Figueiredo et al. reported an average deformation at maximum tensile stress of 0.26% and 0.15%, the results of Mix A demonstrate an average deformation of 0.91%. Mix B, with an average deformation at maximum tensile stress of 0.13% clearly demonstrates a weak strain hardening performance.

In regard to the experimental program an interesting outcome resulted from the cross correlation of the UUCT and the buildability test. In the buildability test of Mix B it was indeed found that the wall failed due to elastic buckling, as was predicted by the Suiker model on the bases of the UUCT data. However, the wall clearly outperformed the expected printing height, based on the same UUCT data. This finding was unexpected and suggests that UUCT, whom were performed on only mixed and not printed fresh samples, underestimates the development of the Young's modulus of the printed material over time. This result may be explained by the fact that only the time is considered when estimating the building height, but the additional effects due to

printing, such as the adding of energy and the entrainment of air, are not.

Furthermore, the experimental program used the initial 4-point bending tests to select the two mix designs with the highest potential for strain hardening behaviour. In this selection procedure, the influence of the fresh properties and the effect on the fibre dispersion, were not considered. In this phase of the mix designs, the mixtures contained no VMA and all six mixes showed low viscosity and were easy to cast. Therefore, it is assumed that the influence of the fresh properties on the 4-point bending test results are minimal.

7. Conclusions

The present study was designed to determine the effect of optimal particle size distribution on the buildability of 3D printable strain hardening cementitious composites.

- The optimization of the particle size distribution can indeed contribute to the buildability performance of 3DP-SHCC. Both Mix A and Mix B have sufficiently high initial yield stress σ_0 and therewith showed no plastic failure during buildability tests.
- The Young's modulus has shown to be the critical fresh mechanical parameter for both Mix A and Mix B. For Mix B, this was found during the buildability test where the wall failed due to elastic buckling and this was supported by the Suiker Model based on the UUCT data. For Mix A no failure occurred during the buildability test, but here also the Suiker model indicated the Young's modulus to be the critical fresh property.
- From the research it can be stated that Mix A has potential for the practical application of 3D printing. The mixture showed good stability during pumping phase and tested samples without entrained air voids showed tensile strain capacity up to 1.85%
- The strain hardening capacity of the printed elements was compromised by the air voids entrapped during the pumping phase.
- 3DP-SHCC is sensitive for dynamic segregation in pumping phase, yielding the formation of fibre balls. Resulting in inconsistent fibre distribution throughout the samples, limiting the strain hardening capacity.
- The pump geometry has proven to be a crucial element in the printing process of 3DP-SHCC. Further research on the influence of the pump geometry on the segregation of 3DP-SHCC is an essential next step in the development of SHCC for 3D printing applications.

CRediT authorship contribution statement

Anne Linde van Overmeir: Conceptualization, Methodology, Software, Validation, Investigation, Formal analysis, Data curation, Writing – original draft, Writing – review & editing. **Stefan C. Figueiredo:** Methodology, Writing – review & editing. **Branko Šavija:** Supervision, Writing – review & editing. **Freek P. Bos:** Resources, Supervision, Writing – review & editing. **Erik Schlangen:** Resources, Supervision, Writing – review & editing.

Declaration of competing interest

The authors declare that they have no known competing financial interests or personal relationships that could have appeared to influence the work reported in this paper.

Acknowledgements

This research was funded through the NWO, Netherlands Open Technology Program, project 'High Performance 3D Concrete Printing', grant number 17251. Additionally, we want to thank Karsten Nefs for his contribution during the printing trials and Linda Versteegh, Koen Grisel and Naomi van Hierden for their assistance in the experimental program.

References

[1] T. Wangler, E. Lloret, L. Reiter, et al., Digital concrete: opportunities and challenges, RILEM Tech. Lett. 1 (2016) 67–75.
[2] G. De Schutter, K. Lesage, V. Mechtcherine, et al., Vision of 3D printing with concrete technical, economic and environmental potentials, Cem. Concr. Res. 112 (2018) 25–36.
[3] R.A. Buswell, W.L. de Silva, S. Jones, J. Dirrenberger, 3D printing using concrete extrusion: A roadmap for research, Cem. Concr. Res. 112 (2018) 37–49.
[4] D. Asprone, F. Auricchio, C. Menna, V. Mercuri, 3D printing of reinforced concrete elements: Technology and design approach, Constr. Build. Mater. 165 (2018) 218–231.
[5] T.A. Salet, Z.Y. Ahmed, F.P. Bos, H.L. Laagland, Design of a 3D printed concrete bridge by testing, Virtual Phys. Prototyp. 13 (3) (2018) 222–236.
[6] S. Lim, R. Buswell, T. Le, et al., Development of a viable concrete printing process, in: Proceedings Of The 28th International Symposium On Automation And Robotics In Construction, ISARC 2011, 2011.
[7] V. Li, From micromechanics to structural engineering – the design of cementitious composites for civil engineering applications, J. Struct. Mech. Earthq. Eng. 10 (2) (1993).
[8] V. Li, Engineered Cementitious Composites (ECC), Springer, 2019.
[9] D.G. Soltan, V.C. Li, A self-reinforced cementitious composite for building-scale 3D printing, Cem. Concr. Compos. 90 (2018) 1–13.
[10] S.C. Figueiredo, C.R. Rodriguez, Z.Y. Ahmed, et al., An approach to develop printable strain hardening cementitious composites, Mater. Des. 169 (2019) 107651.
[11] H. Ogura, V. Nerella, V. Mechtcherine, Developing and testing of strain-hardening cement-based composites (SHCC) in the context of 3D-printing, Materials 11 (8) (2018) 1375.
[12] B. Zhu, J. Pan, B. Nematollahi, et al., Development of 3D printable engineered cementitious composites with ultra-high tensile ductility for digital construction, Mater. Des. 181 (2019) 108088.
[13] V. Li, F.P. Bos, K. Yu, et al., On the emergence of 3D printable engineered, strain hardening cementitious composites (ECC/SHCC), Cem. Concr. Res. 132 (132) (2020).
[14] T. Le, S. Austin, S. Lim, Mix design and fresh properties for high-performance printing concrete, Mater. Struct. 45 (2012) 1221–1232.
[15] J. Kruger, S. Zeranka, G. van Zijl, Rheo-Mechanics Modelling of 3D Concrete Printing Constructability (Ph.D. thesis), Stellenbosch University, 2019.
[16] V.C. Li, On engineered cementitious composites (ECC), J. Adv. Concr. Technol. 1 (3) (2003) 215–230.
[17] N. Roussel, Rheological requirements for printable concretes, Cem. Concr. Res. 112 (2018) 76–85.
[18] D. Marchon, S. Kawashima, H. Bessaies-Bey, S. Mantellato, S. Ng, Hydration and rheology control of concrete for digital fabrication: Potential admixtures and cement chemistry, Cem. Concr. Res. 112 (2018) 96–110.
[19] S. Chaves Figueiredo, C. Romero Rodriguez, Z. Ahmed, D. Bos, Y. Xu, T. Salet, O. Çopuroğlu, E. Schlangen, F. Bos, Mechanical behavior of printed strain hardening cementitious composites, Materials 13 (2020).
[20] J. Zhou, S. Qian, M. Guadalupe Sierra, et al., Development of engineered cementitious composites with limestone powder and blast furnace slag, Mater. Struct. 43 (2010) 803–814.
[21] J. Kruger, S. Zeranka, G. van Zijl, An ab initio approach for thixotropy characterisation of (nanoparticle-infused) 3D printable concrete, Constr. Build. Mater. 224 (2019) 372–386.
[22] N. Roussel, et al., Understanding The Rheology Of Concrete, Woodhead publishing, 2012.
[23] L. Reiter, T. Wangler, N. Roussel, R.J. Flatt, The role of early age structural build-up in digital fabrication with concrete, Cem. Concr. Res. 112 (2018) 86–95.
[24] J. Kruger, S. Zeranka, G. van Zijl, Quantifying constructability performance of 3D concrete printing via rheology-based analytical models, in: Rheology And Processing Of Construction Materials, Springer, 2019, pp. 400–408.
[25] Y. Zhang, Y. Zhang, W. She, et al., Rheological and harden properties of the high-thixotropy 3D printing concrete, Constr. Build. Mater. 201 (2019) 278–285.
[26] Z. Quanji, Thixotropic Behavior of Cement-Based Materials: Effect of Clay and Cement Types, Iowa State University, 2010.
[27] H. Brouwers, H. Radix, Self-compacting concrete: The role of the particle size distribution, Trans. Soc. Mod. Simul. Int. Simul. (2005).
[28] S. Kumar, M. Santhanam, Particle packing theories and their application in concrete mixture proportioning: A review, Indian Concr. J. 77 (2003) 1324–1331.
[29] D.D. J.E. Funk, Predictive Process Control of Crowded Particulate Suspensions: Applied to Ceramic Manufacturing, Springer, 1994.
[30] X. Wang, K. Wang, P. Taylor, G. Morcous, Assessing particle packing based self-consolidating concrete mix design method, Constr. Build. Mater. 70 (2014) 439–452.
[31] K. Ragalwar, W.F. Heard, B.A. Williams, et al., Significance of the particle size distribution modulus for strain-hardening-ultra-high performance concrete (SH-UHPC) matrix design, Constr. Build. Mater. 234 (2020) 117423.

[32] K.A. Ragalwar, H. Nguyen, R. Ranade, W.F. Heard, B.A. Williams, Influence of distribution modulus of particle size distribution on rheological and mechanical properties of ultra-high-strength SHCC matrix, in: V. Mechtcherine, V. Slowik, P. Kabele (Eds.), Strain-Hardening Cement-Based Composites, Springer Netherlands, Dordrecht, 2018, pp. 221–229.
[33] S. Fennis, J. Walraven, Using particle packing technology for sustainable concrete mixture design, Heron 57 (2012).
[34] A.R. Arunothayan, B. Nematollahi, R. Ranade, S.H. Bong, J. Sanjayan, Development of 3D-printable ultra-high performance fiber-reinforced concrete for digital construction, Constr. Build. Mater. 257 (2020) 119546.
[35] A. Andreasen, J. Andersen, Ueber die beziehung zwischen Kornabstufung und Zwischenraum in Produkten aus losen Körnern (mit einigen experimenten, Kolloid Z. 50 (1930) 217–228.
[36] D. Kumar, K. Ragalwar, W. Heard, B. Williams, R. Ranade, Influence of maximum aggregate size and distribution modulus on UHPC matrix properties, 2020.
[37] J. Benbow, J. Bridgwater, Paste flow and extrusion, in: Oxford Series On Advanced Manufacturing, Clarendon Press, 1993.
[38] R. Wolfs, Experimental Characterization and Numerical Modelling of 3D Printed Concrete: Controlling Structural Behaviour in the Fresh and Hardened State (Ph.D. thesis), Technische Universiteit Eindhoven, 2019, Proefschrift.
[39] ASTM D2166-00, Standard Test Method for Unconfined Compressive Strength of Cohesive Soil, ASTM International, 2000, www.astm.org.
[40] R.J.M. Wolfs, A.S.J. Suiker, Structural failure during extrusion-based 3D printing processes, Int. J. Adv. Manuf. Technol. 104 (1–4) (2019) 565–584.
[41] J. Kruger, S. Zeranka, G. van Zijl, 3D concrete printing: A lower bound analytical model for buildability performance quantification, Autom. Constr. 106 (2019) 102904.
[42] A. Suiker, Mechanical performance of wall structures in 3D printing processes: theory, design tools and experiments, Int. J. Mech. Sci. 137 (2018) 145–170.
[43] ASTM C39/C39M-17, Standard Test Method for Compressive Strength of Cylindrical Concrete Specimens, ASTM International, 2017, www.astm.org.
[44] A.L. van Overmeir, Designing an Interlayer Reinforcement Solution for Printable Strain-Hardening Cement-Based Composites, Delft University of Technology, 2020.
[45] S. Chaves Figueiredo, A.L. van Overmeir, K. Nefs, et al., Quality assessment of printable strain hardening cementitious composites manufactured in two different printing facilities, in: Second RILEM International Conference on Concrete and Digital Fabrication, Springer International Publishing, 2020, pp. 824–838.